An Enigmatic X-Ray Binary: Cygnus X-3

Bharadwaj Varma P K

MS15166

Under the guidance of

Dr. Aru Beri

A thesis presentation submitted for BS-MS Dual Degree in Science

Department of Physical Sciences

Indian Institute of Science Education and Research

Jan 2020

Certificate of Examination

This is to certify that the dissertation titled "An Enigmatic X-Ray Binary : Cygnus X-3" submitted by Mr.Bharadwaj Varma P K (Reg. No. MS15166) for the partial fulfilment of BS-MS dual degree programme of the Institute, has been examined by the thesis committee duly appointed by the Institute. The committee finds the work done by the candidate satisfactory and recommends that the report be accepted.

Dr. K P Singh   Dr. J S Bagla   Dr. A Shivaji   Dr. Aru Beri

(Supervisor)

Dated On

Declaration

The work presented in this dissertation has been carried out by me under the guidance of Dr.Aru Beri at the Indian Institute of Science Education and Research Mohali. This work has not been submitted in part or in full for a degree, a diploma, or a fellowship to any other university or institute. Whenever contributions of others are involved, every effort is made to indicate this clearly, with due acknowledgement of collaborative research and discussions. This thesis is a bonafide record of original work done by me and all sources listed within have been detailed in the bibliography.

Bharadwaj Varma

(Candidate)

Dated on

In my capacity as the supervisor of the candidate's project work, I certify that the above statements by the candidate are true to the best of my knowledge

Dr. Aru Beri

(Supervisor)

Acknowledgement

Abstract

With this thesis, I aimed at learning tools and techniques used in X-ray astronomy. X-ray Astronomy is a branch of astronomy where observations are performed using space missions as X-rays cannot penetrate the Earth's atmosphere. Over this period, I have learnt about different physical/emission processes that are responsible for the generation of X-rays in the sky. I have learnt detection tools and techniques that are used.

In particular, I have been involved in studying a particular X-ray source, Cyg X-3 which belongs to the class of X-ray sources named as X-ray Binaries. Cyg X-3 is an interesting source located in the Cygnus constellation. One of the key characteristics of this source is that it not only X-ray bright but very luminous in other electromagnetic bands (radio, optical, gamma-rays) as well. Hence, it is a target of interest to perform a multi-wavelength study.

In our work, we have used optical (from All Sky Automated Survey for Supernovae) and X-ray data (Neil Gehrels Swift Observatory and Monitor of All-Sky X-Ray Image) to perform our studies.

In particular, I have used 3 years of X-ray and optical data to understand the long term spectral evolution of this source. A model-independent way (hardness ratio) was used for the purpose. We found that there exist an anti- correlation between hard and soft X-rays but optical emission is independent of any such correlation. The source was found to be optically bright throughout during the period of three years, starting from 2015.

In addition, we have also used pointed observations of this source made with NASA's observatory, NuSTAR. Using the long-term light curves with Swift and MAXI, we noticed that the pointed observation of Cyg X-3 used in this work was performed during its hypersoft spectral state. The X-ray light curves obtained with NuSTAR showed a large variability. Therefore, in order to investigate the evolution of spectral parameters with time, we have performed a time-resolved spectroscopy. Our preliminary results revealed

large variability in the X-ray flux. However, no significant variation was found in neutral hydrogen column density, optical depths of absorption edges found in the X-ray spectra. In future, we aim at performing a more detailed and careful spectral study of this source to obtain physical insights of the geometry of this system.

Contents

List of Figures

List of Tables

Chapter 1

Introduction

1.1 Introduction to X-Ray Astronomy

Figure 1.1: Electromagnetic Spectrum (*Electromagnetic Spectrum - Introduction* 2013)

X-Rays occupy the frequency range of $3 \times 10^{16} - 3 \times 10^{19}$ Hz in the electromagnetic spectrum. In terms of energy, they occupy the energy band of E = 0.1 - 100 keV. The soft

X-Rays are of energies from 0.1 to 10 keV and the hard X-Rays are of energies 10 to 100 keV

It is impractical and almost impossible to observe astronomical X-Rays using ground based equipment because our atmosphere is opaque to X-Rays, i.e. the X-Rays do not penetrate the atmosphere below roughly 30km of altitude. So its observation is carried out above the atmosphere. (See Fig 1.1)

1.2 How X-rays are produced in the Sky?

In this section, different emission processes describing the production of X-Rays will be discussed. The main processes are thermal bremsstrahlung, synchrotron radiation, inverse Compton scattering, blackbody radiation.

1.2.1 Bremsstrahlung

Bremsstrahlung or braking radiation, is similar to free-free emission because electrons are free before and after their interaction with ions. We consider a scenario in which high speed electrons move past stationary nuclei. Throughout this motion, the electron experiences the Coulomb field of the nucleus.

To find the spectrum of Bremsstrahlung, we need to take the Fourier transform of the acceleration. The electrostatic acceleration of the electron in rest frame is given by :

$$a_\parallel = \dot{v}_x = -\frac{eE_x}{m_e} = \frac{\gamma Z e^2 v t}{4\pi\epsilon_0 m_e [b^2 + (\gamma v t)^2]^{\frac{3}{2}}} \tag{1.1}$$

Similarly, for the perpendicular component,

$$a_\perp = \dot{v}_z = -\frac{eE_z}{m_e} = \frac{\gamma Z e^2 b}{4\pi\epsilon_0 m_e [b^2 + (\gamma v t)^2]^{\frac{3}{2}}} \tag{1.2}$$

where, b is the impact parameter between the electron and nucleus. This is derived from the relativistic transformation of the inverse square law Coulomb field.

 After taking the Fourier transfrom, we obtain the following formula,

$$\dot{v}_x(\omega) = \frac{1}{\sqrt{2\pi}} \frac{Ze^2}{4\pi\epsilon_0 m_e} \frac{1}{\gamma b v} I_1(y) \tag{1.3}$$

$$\dot{v}_z(\omega) = \frac{1}{\sqrt{2\pi}} \frac{Ze^2}{4\pi\epsilon_0 m_e} \frac{1}{bv} I_2(y) \tag{1.4}$$

where $y = \frac{\omega b}{\gamma v}$ and

$$I_1(y) = 2iyK_0(y) \tag{1.5}$$

$$I_2(y) = 2iyK_1(y) \tag{1.6}$$

where K_0 and K_1 are modified Bessel function of order 0 and 1. Hence, the spectrum obtained will be of the form,

$$I(\omega) = \frac{Z^2 e^6}{24\pi^6 \epsilon_0^3 c^3 m_e^2 v^2} \frac{\omega^2}{\gamma^2 v^2} [\frac{1}{\gamma^2} K_0^2(\frac{\omega b}{\gamma v}) + K_1^2(\frac{\omega b}{\gamma v})] \tag{1.7}$$

For viewing the spectrum, see Fig.1.2
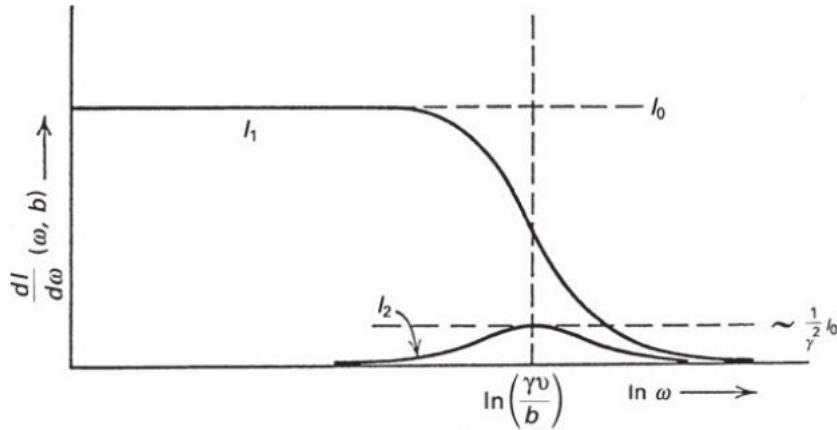
Figure 1.2: Spectrum of Bremsstrahlung. Image taken from (Longair, 2011)

For astrophysical situations, we need to look at the spectrum of a thermal plasma (See 1.2). So we integrate the single particle spectrum over collision parameters and a Maxwellian distribution of electrons.

$$N_e(v)dv = 4\pi N_e (\frac{m_e}{2\pi kT})^{3/2} v^2 e^{\frac{-m_e v^2}{2kT}} dv \tag{1.8}$$

We replace, $\frac{m_e v^2}{2}$ with $\frac{3}{2}kT$

Thus the spectrum obtained is :

$$I(\omega) = \frac{Z^2 e^6 N N_e}{12\sqrt{3}\pi^3 \epsilon_0^3 c^3 m_e^2} \left(\frac{m_e}{kT}\right)^{\frac{1}{2}} g(\omega, T) \tag{1.9}$$

where m_e is the mass of electron, N_e is the number density of electrons, Ze is the charge of the interacting ion, k is the Boltzmann constant, T is the Temperature of the plasma, ω is the frequency of the photon and $g(\omega, T)$ is called Gaunt factor. Gaunt factor is a quantum mechanical multiplicative correction applied to results related to emission or absorption.

In the low frequency limit, the spectrum becomes almost independent of the frequency, the dependency lying on the Gaunt factor which slowly varies with ω. (see Longair, 2011, for more details)

1.2.2 Synchrotron Radiation

When ultra relativistic electrons pass through a magnetic field, it is further accelerated and thus energy is radiated. This radiation is known as magnetic braking or synchrotron radiation. In the presence of a magnetic field, mobile electrons follow a spiral path at constant pitch angle. This motion is called gyration. The electron gyrates at a frequency(ν_g) :

$$\nu_g = \frac{eB}{2\pi\gamma m_e} \tag{1.10}$$

where B is the magnetic flux density, γ is the Lorentz factor, e is the charge of the elctron and m_e is mass of the electron.

Since electron accelerates towards the guiding centre, there is a radiation which can be obtained from the Larmors formula :

$$-\left(\frac{dE}{dt}\right) = \frac{q^2 a^2}{6\pi\epsilon_0 c^3} \tag{1.11}$$

So, the equation for energy loss rate is obtained from the treatment of particles moving at relativistic velocities. Its acceleration four-vector is given by :

$$\vec{A} = \gamma\left[c\frac{\partial\gamma}{\partial t}, \frac{\partial\gamma v}{\partial t}\right] \tag{1.12}$$

Substituting the expression for acceleration in Larmor's formula, we obtain the following equation :

$$-\left(\frac{dE}{dt}\right) = \frac{q^2\gamma^4}{6\pi\epsilon_0 c^3}[a_\perp^2 + \gamma^2 a_\parallel^2] \tag{1.13}$$

But $a_\parallel = 0$ and $a_\perp = \frac{e\vec{v}B sin\alpha}{\gamma m_e}$. Hence :

$$-(\frac{dE}{dt}) = \frac{e^4 B^2}{6\pi\epsilon_0 cm_e^2} \frac{v^2}{c^2}\gamma^2 sin^2\alpha \tag{1.14}$$

It can be further reduced to :

$$-(\frac{dE}{dt}) = 2\sigma_T c U_{mag}\gamma^2 sin^2\alpha \tag{1.15}$$

where $\sigma_T = \frac{e^4}{6\pi\epsilon_0^2 c^4 m_e}$ is the Thomson scattering cross section, α is the pitch angle, U_{mag} is the energy density of the magnetic field.

Now, we can get asymptotic expressions for the spectral emissivity for synchrotron radiation. In the high frequency limit, it goes as :

$$j(\nu) \propto \nu^{\frac{1}{2}} e^{-\frac{\nu}{\nu_c}} \tag{1.16}$$

Thus it is dominated by an exponential cutoff at $\nu >> \nu_c$. In the low frequency limit,

$$j(\nu) \propto \nu^{\frac{1}{3}} \tag{1.17}$$

1.2.3   Blackbody Radiation
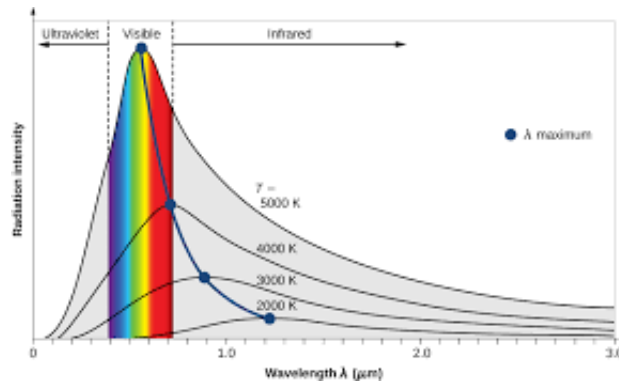
Figure 1.3: Blackbody Radiation Spectrum. See (Ling, Sanny, and Moebs, 2016)

A blackbody absorbs all kinds of electromagnetic radiation and emits all of them, that is, there is zero reflection. At constant temperature, blackbody radiation is in thermal equilibrium with matter. The blackbody spectrum can be described by the Planck function given by :

$$B_\nu(T) = (\frac{2h\nu^3}{c^2})\frac{1}{e^{\frac{h\nu}{kT}} - 1} \tag{1.18}$$

where, ν is the frequency of radiation, h is the Planck's constant, T is the temperature of the source. Blackbody radiation lies in the X-Ray region, if the temperature of the blackbody is of the order 10^6 K.

1.3 How Do X-Rays Interact With Matter ?

1.3.1 Photoelectric Absorption

This mainly happens when the photons are of low energies, much lesser than their rest mass energy. It is also called bound-free absorption since the electron is initially bound and is then set free after the interaction. When the energy of the incident photons exceed that of the first X-Ray atomic energy level, the bound electron is ejected from that energy level. This is what is known as photoelectric effect. Thus, in the spectrum of radiation we observe an edge, known as absorption edge, if the photon energy matches the atomic energy level. If the edge is formed due to the ejection of a K-Shell electron, then it is called a K-edge.

In the X-Ray range of electromagnetic spectrum, atoms absorb X-Rays primarily by photoelectric absorption of X-Ray photons. It is followed by an emission of an electron from the atom and leaves behind an ion and an excited atom. This excited atom eventually de-excites with the emission of a photon with an energy characteristic of atomic energy levels. These levels are also called shells and they are designated the letters starting from K, L, M, etc. The equation of photoelectric absorption is given by :

$$h\nu - \phi = E_{max} \tag{1.19}$$

where $h\nu$ is the energy fo the incoming photon, ϕ is the binding energy of the electron to the atom and E_{max} is the maximum kinetic energy with which the electron is emitted.

Most probably, the electron to be ejected is the one deep in the potential well of the atom. The cross-section of photoelectric absorption can be calculated using methods in Quantum Mechanics. For instance, for photons with $h\nu > E_I$, where E_I is the energy of the atomic level I and $h\nu < m_e c^2$, that is the ejection of electron from K-shell of atoms is given by :

$$\sigma_K = 4\sqrt{2}\sigma_T \alpha^4 Z^5 \left(\frac{m_e c^2}{h\nu}\right)^{\frac{7}{2}} \tag{1.20}$$

where σ_T is the Thomson cross-section which will be discussed in the next section. Since the absorption cross-section is heavily dependent on Z, heavier elements which are rare contribute significantly to photoelectric absorption. For multiple elements, the total photoelectric absorption is added and weighted by cosmic abundances of other elements with respect to hydrogen.

$$\sigma_e(E) = \frac{1}{n_H}\Sigma_i n_i \sigma_i(E) \tag{1.21}$$

1.3.2 Thomson Scattering

It describes the scattering of unpolarised beam of radiation by an electron. The electromagnetic wave, in this case, is scattered without change in energy, as it happens in the low energy limit.

The total scattered radiation into a solid angle is obtained by the Larmor's formula :

$$-(\frac{dE}{dt})d\Omega = \frac{e^4 E_x^2}{16\pi^2\epsilon_0 c^3 m_e^2}cos^2\alpha d\Omega \tag{1.22}$$

We also substitute the Poynting vector, $S_x = c\epsilon_0 E_x^2 i_z$ This is loss along x-direction. Similarly we work out for y-direction and sum both the results to get the total energy loss :

$$-(\frac{dE}{dt})d\Omega = \frac{e^4}{16\pi^2 m_e^2\epsilon_0^2 c^4}(1 + cos^2\alpha)\frac{S}{2}d\Omega \tag{1.23}$$

where S is the magnitude of the Poynting vector, α is the scattering angle.

To get the scattering cross-section, we get the scattered intensity in terms of $d\sigma_T$ in the direction of α. Thus we get an expression of the form :

$$d\sigma_T = \frac{r_e^2}{2}(1 + \cos^2\alpha)d\Omega \tag{1.24}$$

Integrating it over all solid angles we get the total cross-section as :

$$\sigma_T = \frac{e^4}{6\pi\epsilon_0^2 m_e^2 c^4} = 6.653 \times 10^{-29} m^2 \tag{1.25}$$

1.3.3 Compton Scattering

It is the high energy version of Thomson Scattering. High energy photons are scattered to lower energies by stationary electrons as they transfer their kinetic energy to the electrons.

The change in the wavelength of photons are given by :

$$\frac{\Delta\lambda}{\lambda} = \frac{\hbar\omega}{m_e c^2}(1 - cos\alpha) \tag{1.26}$$

Thomson scattering cross section is only used for cases where electron velocities are much lesser than c or if photon energies are much less than the rest mass energy of the electrons.

1.3.4 Inverse Compton Scattering

In this scenario, the electrons move at ultra-relativistic speeds, that is speeds close to c. These electrons when encountered with low energy photons, scatter them to higher energies at the expense of its kinetic energy. For this case, we consider a situation where the photon energy in centre of momentum frame $< m_e c^2$ and thus the Thomson scattering cross section is used to describe its scattering probability. So the energy loss rate will take the form : (Longair, 2011)

$$-(\frac{dE}{dt}) = \sigma_T c u'_{rad} \tag{1.27}$$

where u'_{rad} is the energy density of radiation of the electron in its rest frame. Now,

$$du'_{rad} = u_{rad}\gamma^2[1 + (v/c)cos\theta]^2 d\Omega \tag{1.28}$$

Now we integrate over the solid angle to obtain :

$$u'_{rad} = \frac{4}{3}u_{rad}(\gamma^2 - \frac{1}{4}) \tag{1.29}$$

Substituting this we get the energy gained by the photon field when low energy photons are scattered.

$$\frac{dE}{dt} = \frac{4}{3}c\sigma_T u_{rad}(\gamma^2 - \frac{1}{4}) \tag{1.30}$$

To obtain, the total energy gained by the photon field, we subtract the initial energy of low energy photons and thus, the energy loss rate for Inverse Compton Scattering is given by :

$$(\frac{dE}{dt}) = \frac{4}{3}\sigma_T c u_{rad}(\frac{v^2}{c^2})\gamma^2 \tag{1.31}$$
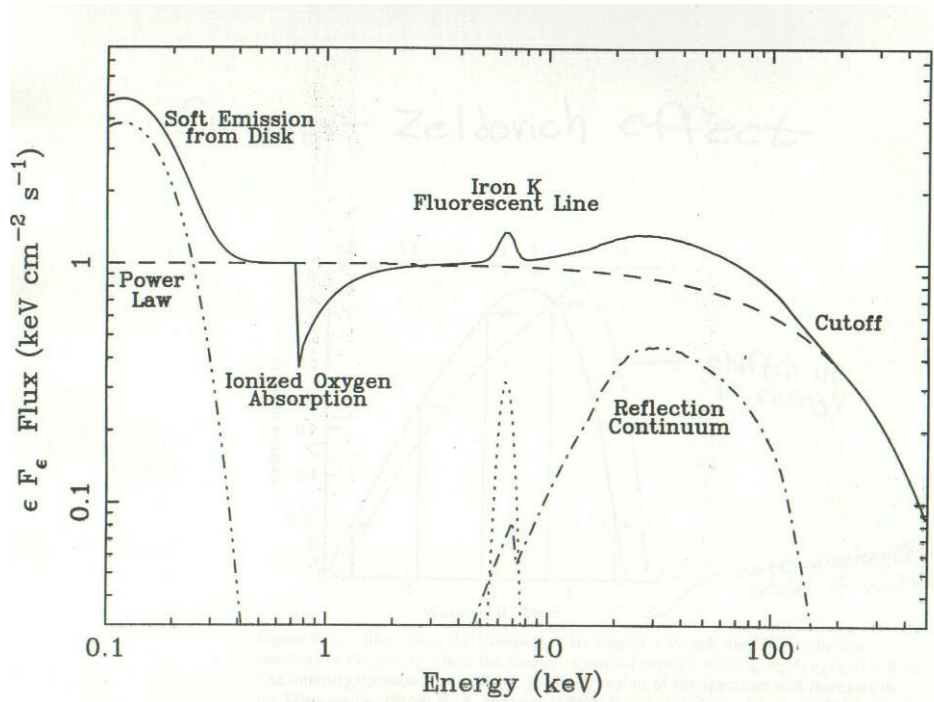
Figure 1.4: Spectrum showing all physical processes. See (Brandt, 2019)

1.4 X-Ray Binaries

Here, in this thesis, we will be focussing on the study of class of objects known as X-ray binaries. X-Ray Binaries are spectroscopic binaries. They usually consists of a compact object in orbit with another star. They emit radiation majorly in the X-Ray regime. Based on the mass of the companion star, that is the star which provides mass to the compact object, they are classified into - High Mass X-Ray Binaries and Low Mass X-Ray Binaries. See (Seward and Charles, 2010)

1.4.1 High Mass X-Ray Binaries

For High Mass X-Ray Binaries or HMXBs, mass of the donor star is in the range $10M_\odot - 100M_\odot$. HMXBs can then be divided into two sub classes based on the donor star :

1) Be XRBs :

These XRBs have a Be Star as a donor, that is a star with hydrogen emission lines. It has luminosity classes III, IV and V. Accretion is either by stellar wind capture or by Roche Lobe Overflow. See (Seward and Charles, 2010)

2) OB Supergiants :

They are of Luminosity classes I and II. These stars lose mass at large rates : $10^{-6}M_{\odot}yr^{-1}$. HMXBs having OB Supergiants generally, accrete via the mechanism of stellar wind capture.

Stellar Wind Accretion in High Mass X-Ray Binaries

In OB stars, the line scattering of radiation produces the strong stellar wind, which is driven due to the action of radiation pressure from the companion star's photosphere. The X-Ray properties of the XRB like flux and spectral changes when the compact object is eclipsed is utilised to observe the stellar wind structure. There are two possibilities :

1) When the stellar wind is dense and not ionised - changes the observed spectrum by attenuating soft X-Rays from the source.

2) When the stellar wind materials are completely ionised due to the extreme brightness of the source. Thus X-Rays aren't absorbed by the gas and spectrum won't be affected.

When there is no ionisation, the velocity profile produced by the driving force is : (Blondin et al., 1990)

$$v_w = v_\infty (1.0 - \frac{R_*}{R})^\beta \qquad (1.32)$$

where v_∞ is the final velocity of the material, R_* is the radius of the OB star and β is a factor which lies between 0.8 and 1.2

If we consider M_x to be the mass of the compact star, which moves in an orbit with velocity v_x. We assume that the stellar wind is radial with velocity v_W. Now, let the velocity of wind with respect to the star be :

$$v_t^2 = v_x^2 + v_W^2 \qquad (1.33)$$

We treat this problem in a way we treat the path of a charged particle passing near to another stationary charge. We consider its impact parameter. Now, the gravitational force
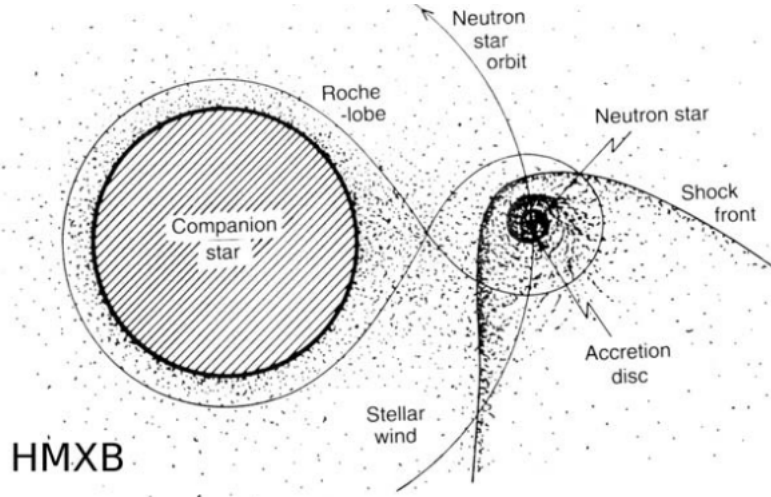
Figure 1.5: Stellar wind accretion in a HMXB. Image taken from (Seward and Charles, 2010)

per mass at impact parameter 'b' is : $\frac{GM_x}{b^2}$

Hence, the impulse is given by :

$$\delta p = \frac{2GM_x}{bv_t} \tag{1.34}$$

Thus, the outflowing wind is deflected towards the axis of the flow. At some distance l downstream, the particles with collision parameter 'b' collide on axis of flow. The perpendicular component of velocity is 0.Thus, the capture radius, or the radius within which matter is definitely captured by the accretor is obtained by equating gravitational potential to its outward kinetic energy per mass :

$$\frac{GM_x}{R_c} = \frac{(v_t)^2}{2} \tag{1.35}$$

where v_t is velocity of wind relative of star and is given by $v_x^2 + v_w^2$.

Thus,

$$R_c = \frac{2GM_x}{v_x^2 + v_w^2} \tag{1.36}$$

where M_x is the mass of the compact object, v_x is velocity of compact object and v_w is velocity of the stellar wind. See (Longair, 2011)

1.4.2   Low Mass X-Ray Binaries

For Low Mass X-Ray Binaries or LMXBs, the accretor is usually a compact object and the donor is usually a main sequence star, with mass in the range : $0.1M_\odot - 1M_\odot$. The

mass transfer is mainly through Roche Lobe Overflow. See (Carroll and Ostlie, 2017)

For the study of Roche Lobe Overflow, we look at the situation as a 3-Body Problem wherein the third object which is very low in mass is in the gravitational potential of the other two massive bodies(stars). Now we have to make two major assumptions :

1) The 2 stars are in circular orbit about each other.

2) We need to treat them as point masses when we see the dynamics.

The major equation in gas dynamics is Euler equation. It is an analogue of Newton's Second Law for a continuous fluid. It is given by :

$$\rho\frac{\partial v}{\partial t} + \rho v.\nabla v = -\nabla P + f$$

where ρ is the density, v is the velocity, P is the pressure of the fluid at each point and f is any other force acting on it per unit volume.

Since all accreting matter is in gaseous form, we use this equation in a frame of reference rotating with the binary system. Thus it becomes :

$$\frac{\partial v}{\partial t} + v.\nabla v = -\nabla \phi_R - 2\omega \wedge v - \frac{1}{\rho}\nabla P$$

where $-\nabla \phi_R$ is called the Roche Potential and $-2\omega \wedge v$ is the Coriolis force. The Roche potential is given by :

$$\phi_R = \frac{-GM_1}{|r - r_1|} - \frac{-GM_2}{|r - r_2|} - \frac{1}{2}(\omega \wedge r)^2$$

where r_1 and r_2 are the position vectors of the centres of the two stars and M_1 and M_2 are their respective masses.

We can draw the equipotential surfaces of ϕ_R. As stated earlier we approximate the two objects to be point masses for large distances. Near the centre of each star, the equipotential surface is circular. This is because at these points, the gravitational pull of the star is very dominating for the matter around it. There is a critical surface where the valleys formed due to the gravitational pull meets, this is called the Roche lobe and the point where they meet is the Inner Lagrangian Point L_1. Material near L_1 escapes into the other
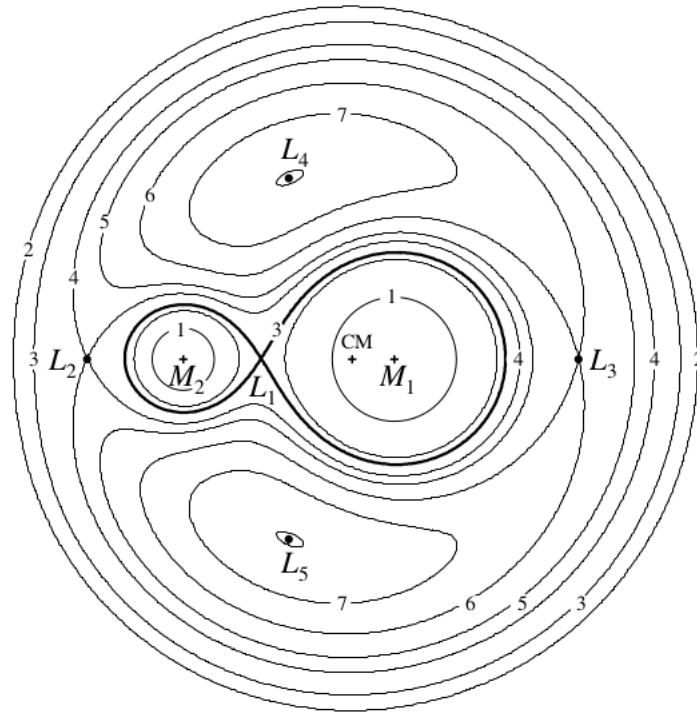
Figure 1.6: Orbital plan of the Roche equipotentials. They are labelled from 1 to 7. L1-L5 Lagrange Points are marked. The inner Lagrangian point L1 is the passage between the two Roche lobes. Image taken from (Frank, King, Raine, et al., 2002)

lobe easily.

In the beginning, both stars would be lesser in size than its Roche Lobe. Thus the surface of each star complies to that of the circular equipotential surface. Therefore, material cannot be influenced by the gravitational pull of the other star. This kind of binary is called detached binary. Now if one star, on its due course of evolution fills its Roche lobe, the part of the envelope of the star lies near to the inner Lagrangian point. The material in the vicinity of L_1 with any perturbation will go through L_1 and into the lobe of the other star. These kind of binaries are called semi-detached binaries and when mass is transferred in this way, that is when one star is in contact with its Roche lobe its called Roche Lobe Overflow. And when both the stars fill their Roche lobes, they are called Contact Binaries. See Figure 1.6

1.5 Basic Accretion Physics

1.5.1 Accretion Discs

As explained above, in the case of Roche lobe overflow, matter is passed through L_1 like it is ejected through a rotating nozzle. Hence the transferred mass has high specific angular momentum. So it does not directly accrete onto the other star. The gas stream is at nearly supersonic speed. Its trajectory can be approximated to that of a particle released from rest at L_1 falling in the gravitational field of the mass capturing star. To fall onto the star, the gas stream needs to get rid of its high angular momentum and thus it tends to form an orbit of the lowest energy - circular orbit. If it were a single test particle, it would have had an elliptical orbit but since its a continuous stream of gas, it will be a ring/disc. When gaseous stream intersect or collide, shocks are created which are dissipative. This dissipative energy is converted into internal energy and a part of it is radiated. A spiralling in of gas occurs due to the loss of angular momentum required to meet the energy losses that is radiated away. The spiralling requires loss of angular momentum, so it is transported to the outer regions which gain angular momentum and thus the outer region spirals out.

1.5.2 Thin Disc Approximation

For thin discs, consider steady accretion into an optically thick but geometrically thin disc. Now, the transferred matter forms orbits around the compact object, which would have been Keplerian if there are no viscous forces present. Now, since incoming matter has large angular momentum, it is difficult for matter to move inwards.

The condition for taking up the thin disc model is that the rotational velocity of disc is much greater than speed of sound. See (Frank, King, Raine, et al., 2002)

The rate of accretion, which is constant is given by:

$$\dot{m} = 2\pi r v_r \Sigma \tag{1.37}$$

where Σ is the surface density, v_r is velocity of inflow.

Applying torque conditions, we get:

$$\nu\Sigma = \frac{\dot{m}}{3\pi}[1 - (\frac{r_*}{r})^{\frac{1}{2}}]$$
(1.38)

The rate of energy dissipation by viscous forces is given by :

$$-(\frac{dE}{dt}) = \frac{3G\dot{m}M_*}{4\pi r^3}[1 - (\frac{r_*}{r})^{\frac{1}{2}}]$$
(1.39)

1.5.3 Emission from Accretion Discs

The emission from the thin disc can be approximated to that of a blackbody radiation at each point in the disc. So equating it to the Stefan's Law for Blackbody Radiation, we can get the temperature of the disc. We have to keep in mind that the disc radiates from both of its surfaces and thus the emission takes the form :

$$\sigma T^4 = \frac{3G\dot{m}M_*}{8\pi r^3}$$
(1.40)

Thus,

$$T = (\frac{3G\dot{m}M_*}{8\pi r^3\sigma})^{\frac{1}{4}}$$
(1.41)

where $\dot{m}$ is accretion rate, Towards the centre, for $r >> r_*$, where r_* is the radius

$$T \propto r^{-\frac{3}{4}}$$
(1.42)

Now we divide, the disc into annuli and we assume that each annulus radiates like a blackbody. Thus we get,

$$I(\nu) \propto \int_{r_1}^{r_{max}} 2\pi r B(T,\nu)dr$$
(1.43)

where $B(T,\nu)$ is the Planck's function. Changing the variable to temperature, we find that the integral is a constant and the final form of intensity as :

$$I(\nu) \propto \nu^{\frac{1}{3}}$$
(1.44)

Now, looking at the extremities, for lower frequencies,

$$I(\nu) \propto \nu^2$$
(1.45)

we get a Rayleigh-Jeans Tail. And for higher frequencies,

$$I(\nu) \propto e^{-\frac{h\nu}{kT_1}}$$
(1.46)

there is an exponential decrease

1.6   X-Ray Spectral States

In (McClintock and Remillard, 2003) and (Remillard and McClintock, 2006), many active states of blackhole binaries have been classified. Before naming them there are some terms to be defined. Disk fraction (f), is the ratio of the flux density of the disc to the total flux density and Γ is the photon spectral index. 'r' is the power density spectrum of variability 0.1 - 10Hz as a fraction of average count rate of source and 'a' is the integrated amplitude of quasi-periodic oscillations which are in the range 0.1-10 Hz. (See Longair, 2011, for more info) The three main spectral states are :

1) Thermal

2) Hard

3) Steep Power Law

The thermal state, is characterised by a disc fraction greater than 0.75. Quasi periodic oscillations are either absent or weak with $a < 0.005$ and $r < 0.075$. The thermal component comes from the inner region of accretion disk. For this case, an optically thick accretion disk model is used. Its temperature distributions is given by :

$$T(r) = [\frac{3GM\dot{m}}{8\pi\sigma r^3}(1 - (\frac{r_i}{r})^{0.5}]^{\frac{1}{4}}$$ (1.47)

where r_i is the inner cut-off radius, $\dot{m}$ is the mass accretion rate.

The hard state is often characterised by the presence of a steady radio jet (McClintock and Remillard, 2003). In the hard state, disc fraction, $f < 0.2$. The photon index lies between 1.4 to 2.1 and value of $r < 0.1$. New investigations have led to believe that the origin of the spectrum is attributed to both synchrotron radiation and Compton scattering.

The steep power law (SPL) state has the following properties : $\Gamma > 2.4$ and $r < 0.15$. It has either a disc fraction less than 0.5 with no quasi periodic oscillations or with $f < 0.8$ with 0.1 - 30 Hz quasi periodic oscillations. This state can produce very high luminosities and a spectra that extends to more than 1 MeV. The steep power law state is explained via the inverse Compton scattering as the mechanism for radiation

1.7 About Cygnus X-3

Cygnus X-3 is a bright and persistent high mass X-Ray binary. The binary system consists of a compact object which is in orbit with a Wolf Rayet star(Fender, Hanson, and Pooley, 1999). It is located near the galactic plane at a distance of 8-10 kpc (Dickey, 1983). A period of 4.8 hours has been observed (Parsignault et al., 1972). (Schmutz, Geballe, and Schild, 1996) derives a mass for the compact object of $7–40 M_\odot$ for a range of Wolf–Rayet masses from 5 to $20 M_\odot$ and inclinations 30–90°, for the mass function of $2.3 M_\odot$.

Cygnus X-3 is considered as a microquasar. Microquasars are characterised by a compact object with an accretion disk and also, a relativistic jet of particles. Thus it also generates radio emission. It undergoes giant radio outbursts. Cygnus X-3 also undergoes γ-ray emissions.

The spectral variability and the geometry of accretion was explained in (Hjalmarsdotter et al., 2009). To describe the continuum, a Comptonisation model is used. This model is described by the upscattering of soft seed photons in a hot flow, which is either located at the inner edge of an accretion disc or on top of the disc. The source of seed photons were assumed to be an accretion disc which has a spectrum of a blackbody. Absorption effects in the stellar wind was also studied in (Hjalmarsdotter et al., 2009) where studies showed the presence of a rich line complex with features corresponding to both absorption and emission at energies lower than 10keV. It was also found that the emission and absorption structure had a requirement of a 2-phase wind made up by a hot plasma along with cool dense clumps. The study also showed strong edge at 7 keV which meant that neutral iron was also present. The edge was due to a combination of neutral absorption and reflection. Another edge was found at 9 keV which comes from iron (highly ionised form) present in the optically thin hot inter-clump wind medium.

1.7.1 Spectral States of Cygnus X-3

The spectral states are divided into five states according to (Szostek and Zdziarski, 2005) : hard state, intermediate state, very high state, soft non-thermal state and the ultrasoft state.
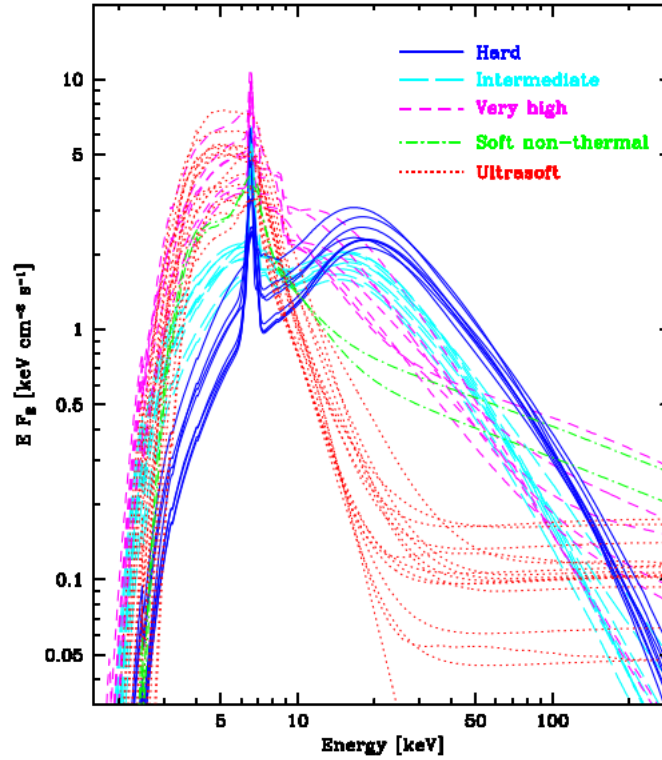
Figure 1.7: Spectral states in five groups, the hard state (blue solid line), the intermediate state (cyan long-dashed line), the very high state (magenta short-dashed line), the soft non-thermal state (green dot–dashed line) and the ultrasoft state (red dotted line). Image from (Hjalmarsdotter et al., 2009)

Hard State

The hard state of Cygnus X-3 has a peak at lower energies than other sources. This cutoff is due to an electron temperature of the Comptonising electrons below 10 keV, which is normally seen in soft states where there is strong cooling as a result of influx of soft seed photons from a strong blackbody component.

Intermediate State

It is usually seen in transition from soft to hard and hard to soft states. The model for intermediate state is similar to hard state, they have almost the same blackbody temperatures but heating of the electrons is balanced by cooling by seed photons. Also, in the spectral shape it has a lower amplitude of reflection in comparison to the hard state.

Very High State

A very high state is characterised by the presence of both a strong blackbody component and a strong component from thermal Comptonization. It maybe similar to the intermediate state in some cases. For Cyg X-3, it is a soft state with the spectrum dominated by a strong Comptonised component.

Soft Non-Thermal State

It is a soft state with a moderate disc component and a strong non-thermal tail. It is modelled using a Comptonized blackbody like that of the very high state, but weaker and a strong non-thermal component requiring an almost 75 per cent non-thermal distribution of the Comptonising electrons.

Ultrasoft State

It is the softest state of Cyg X-3. The soft component dominates the spectrum with only weak emission above nearly 20 keV. This state occurs at high accretion rates where the thin disc extends all the way into the innermost stable orbit of the black hole. A strong non-thermal tail, is also present.

Rajeev et al., 1994 observed Cyg X-3 during its high and low spectral states. The X-Ray continuum radiation was described using a combination of a blackbody and a Comptonisation plasma and the source of X-Ray emission being an accretion disk. The blackbody flux was deemed to be the component with the maximum modulation depth. The blackbody temperature seemed to show mild modulation but significant in the high state. Similarly, the hydrogen column density, N_H showed no significant modulation in the low state but mild in high state. The results showed the presence of a stable accretion disk. They also detected the iron line emission from a highly ionised region. The line emission may occur due to the fluorescence of ionised matter and the large width may arise due to the scattering of high energy electrons in the plasma. The line width gives us the information on parameters like temperature and optical depth of the ionised matter. The line emission is in a very narrow segment on the edge of the thick Comptonised region or in a

cooler scattering region and it originates by impeding X-Ray radiation scattered from the continuum source.

Two iron absorption edges were also observed : Fe I at 7.1 keV and Fe XXV at 9.2 keV. There was significant modulation of the optical depths in the high state. The origin of both neutral and ionised iron absorption may attributed to the different ionisation regions in the outer parts of the accretion disk.

Chapter 2

X-Ray Observatories and Detectors

2.1 Brief History on X-Ray Missions

The advent of X-Ray Astronomy began in the 1950s when Riccardo Giacconi headed his group from American Science and Engineering or ASE to detect X-Ray radiation from the Moon, which is actually energetic solar wind particles struck on the Moon's surface. Then, they launched an instrument on 18 June 1962 from White Sands, New Mexico. It detected a powerful cosmic X-Ray source, which later was named as Sco X-1 since it belongs to the Scorpius constellation. Optically, Sco X-1 was found to be very faint, but it was strong in X-Ray radiation.

After discovering Sco X-1, there were many rocket and balloon experiments to detect more X-Ray sources at stellar distances. In the beginning, the nature of X-Ray source and the emission mechanism was not understood. For this, the exact location of the source should be known and X-Ray spectra and light curves were to be determined. Then, came the big breakthrough after the launch of Uhuru(which means "freedom" in Swahili) or the X-ray Explorer Satellite, SAS-A(Small Astronomy Satellite) on December 12, 1970 from the San Marco platform in Kenya. It operated in the 2-20 keV range and was operational till 1973. Its aims were all sky survey for cosmic X-Ray sources and to get X-Ray variability and spectral features.

In 1971, it was available to detect a powerful X-Ray source in the Centaurus constellation which came to be known as Cen X-3. It was present in the Southern Sky at a declination angle of -60°. It was first observed with a regular periodicity of 4.84 seconds by measuring the X-Ray flux. They also observed rapid pulsations and came to the conclusion that they were rotating neutron stars or pulsars. The neutron star was orbiting a B0Ib star or Krzeminski's star in an eclipsing binary system.

Then came many other research groups like Lockheed, MIT, etc., which detected many bright sources in the plane of the Milky Way galaxy. In 1973, cataclysmic variables or CV were discovered by observing the soft X-Rays coming from SS Cygni, which is actually a white dwarf star orbiting a red dwarf star. It belongs to a class called dwarf nova. After that, X-Ray emissions from supernova remnants (like Crab Nebula) and also from coronal emission from stars were observed. The first extra-galactic source to be observed is M87 active galaxy in the Virgo constellation. In 1990, the ROSAT (Röntgensatellit) mission was successfully launched, which carried an imaging X-Ray telescope and two position sensitive proportional counters. See (Seward and Charles, 2010) for more information

2.2   X-Ray and Optical Observatories

2.2.1   Neil Gehrels Swift Observatory

Neil Gehrels Swift Observatory is a mission from NASA, dispatched for the study of Gamma Ray Bursts. Earlier, it was known as Swift Gamma-Ray Burst Mission, then renamed to its present name after its Principal Investigator, Neil Gehrels. It was launched on November 20, 2004, at 17:16 UTC aboard a Delta II 7320-10C from Cape Canaveral Air Force Station

There are mainly three instruments aboard the observatory :

1) Burst Alert Telescope(BAT):
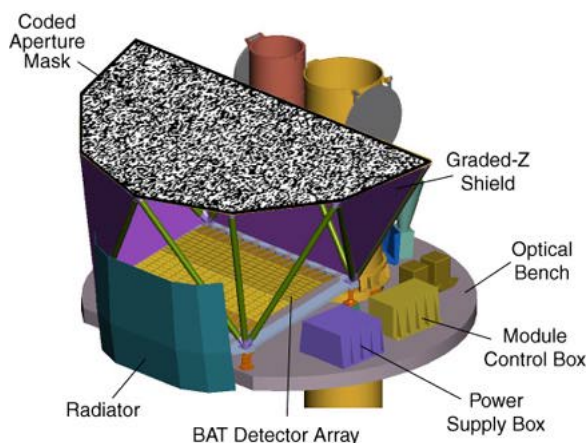
Figure 2.1: BAT schematic (*Swift: About Swift - BAT Instrument Description* 2014)

Burst Alert Telescope detects Gamma Ray Bursts and obtains its coordinates. It works in the energy range 15 - 150 keV. Within several seconds of detecting a burst, the BAT calculates an initial position, decides whether the burst merits a spacecraft slew and, if so, sends the position to the spacecraft. The BAT uses a coded-aperture mask of 52,000 randomly placed 5 mm lead tiles, 1 meter above a detector plane of 32,768 four mm CdZnTe (Cadmium Zinc Telluride) hard X-ray detector tiles. There are two modes of working for the BAT : Burst Mode, where burst positions are obtained and Survey Mode, where hard X-Ray survey data is obtained
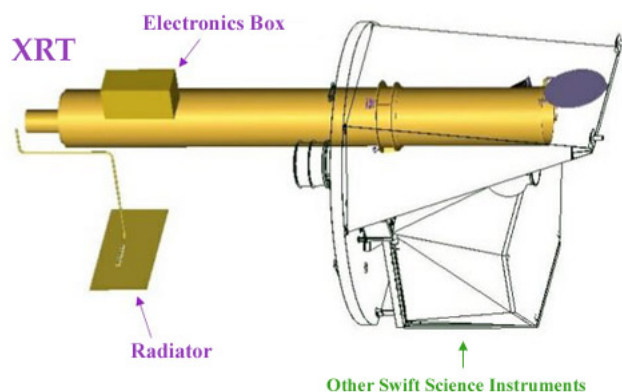
2) X-Ray Telescope(XRT) :

Figure 2.2: XRT schematic (*Swift: About Swift - XRT Instrument Description* 2016)

The X-Ray Telescope works in the energy range of 0.2 - 10 keV, that is, the soft X-Ray waveband. Its main purpose is the analysis of the observed GRBs (Gamma Ray Bursts) and afterglows, that is, it measures the flux and performs spectral analysis. It also performs long-term monitoring of Gamma Ray Burst afterglow light-curves for days to weeks after the event.

The telescope used for XRT is of type, JET-X Wolter I. It has a $110 cm^2$ effective area, 23.6 x 23.6 arcmin FOV, 18 arcsec resolution. It has a single CCD-22 detector. The CCD consists of an image area with 600 x 602 pixels (40 x 40 microns) and a storage region of 600 x 602 pixels (39 x 12 microns).

3) Ultraviolet/Optical Telescope (UVOT) :
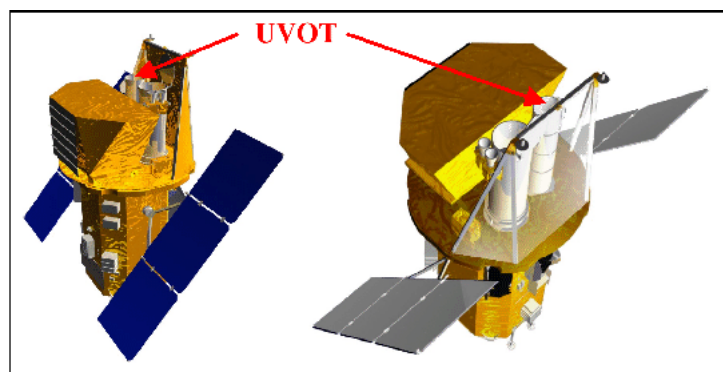
Figure 2.3: UVOT schematic (*Swift: About Swift - UVOT Instrument Description* 2014)

As the name suggests, UVOT work in the Ultraviolet and Optical regime of the spectrum. It is mainly used to observe optical afterglows. UVOT observations enable optimal ground-based observations by providing rapid optical images of the GRB field so that any optical or infrared counterpart can be quickly identified and studied. The telescope employed is a Modified Ritchey-Chrétien type telescope. Ritchey-Chrétien telescopes uses hyperbolic primary and secondary mirrors.

2.2.2   Monitor of All-Sky X-Ray Image (MAXI)

MAXI is an X-Ray Telescope located in the International Space Station. It is part of the Japanese Experimental Module - Exposed Facility. It has started its observations from 15-8-2009 or MJD 55058. It was developed by Japan Aerospace Exploration Agency (JAXA) and is designed to continuously monitor X-ray sources and variability. It has mainly two detectors on-board - the GSC(Gas Slit Camera) and the SSC(Solid-state Slit Camera).

It covers the energy band from 2 to 30 keV. It employs a conventional slit camera that consists of Xe-gas proportional counters and slit-and-slat collimators. Twelve gas counters achieve a large detector area of $5350cm^2$.

The GSC or Gas Slit Camera scans the whole sky with an orbital period of 92 minutes. It operates in the 2 - 30keV band. The GSC has large-area position-sensitive proportional counters with the total detector area of $5350cm^2$. Slit cameras are generally free from the source contamination over the coded-aperture mask while it has a disadvantage in the limited slit area. To achieve the high sensitivity, the large-area proportional counters are filled with Xe gas are used for the X-ray detectors.

Two sets of SSC sensors view X-ray sky using charge-coupled devices (CCDs) in 0.5–12 keV band. The total area for the X-ray detection is about $200cm^2$ which is the largest among the missions of X-ray astronomy. The energy resolution at the CCD temperature of $-70°C$ is 145 eV in full width at the half maximum (FWHM) at 5.9 keV.

2.2.3   NuSTAR

NuSTAR or Nuclear Spectroscopic Telescope Array was launched on June 13 2012. It operates in the region of 3 keV - 79 keV energy band of the electromagnetic spectrum. NuSTAR works on a conical approximation to a Wolter Telescope, which has 133 concentric mirror shells. It has newly developed detectors that extend sensitivity to higher energies as compared to previous missions such as Chandra and XMM. After launching into orbit on a small rocket, the NuSTAR telescope extends to achieve a 10-meter focal length. The observatory will provide a combination of sensitivity, spatial, and spectral resolution factors of 10 to 100 improved over previous missions that have operated at these

X-ray energies.
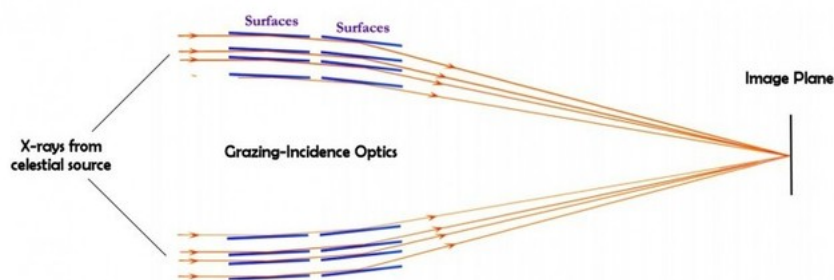
Figure 2.4: NuSTAR grazing incidence (*Optics* 2019)
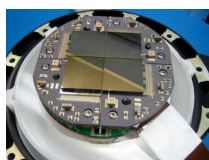
Figure 2.5: NuSTAR focal plane (*Optics* 2019)
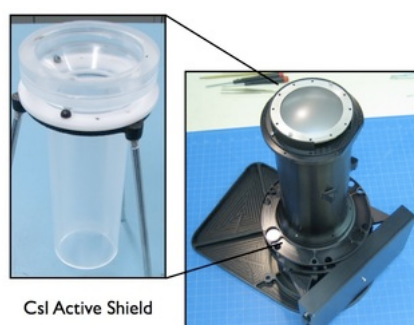
Figure 2.6: NuSTAR CsI shield (*Optics* 2019)

There are mainly three types of Wolter Telescopes : Wolter 1, Wolter 2 and Wolter 3. These are two mirror systems. While Wolter 1 and 2 employ paraboloid-hyperboloid mirror system, Wolter 3 employs a paraboloid-ellipsoid system. To obtain large effective aperture areas Wolter 1 mirrors are nested.

For X-Ray Optics the principle of grazing incidence reflection is used. X Rays are reflected when the angle of incidence is very small and the surface is smooth. Wolter Optics uses this idea. It obeys the Abbey sine condition :

$$\frac{d}{sinv} = f \tag{2.1}$$

CZT or Cadmium Zinc Telluride is a direct bandgap semiconductor detector. They are very efficient at turning high energy photons into electrons. It has better energy resolution than scintillation detectors and a high sensitivity for X-Rays and Gamma Rays

2.2.4   All Sky Automated Survey for Supernovae

All Sky Automated Survey for Supernovae or ASAS-SN is a mission for discovering many bright supernovae. It scans the whole sky every night. ASAS-SN works in the visible range of the electromagnetic spectrum. It comprises of 24 telescopes present around the world. There are six different units for ASAS-SN :

1) Brutus (Las Cumbres Observatory, Hawaii) with 4 robotic telescopes(14-cm)

2) Cassius (Chile) - 4 robotic 14-cm telescopes

3) Cecilia Payne-Gaposchkin (South Africa)

4) Henrietta Leavitt (Texas)

5) Bohdan Paczyński (Chile)

6) Tian Shan (China)

For more information, see (Benjamin J Shappee et al., 2014) and (Kochanek et al., 2017)

Chapter 3

Observations and Data Analysis

3.1 HEASOFT

HEASOFT is a collection of softwares released by the HEASARC or High Energy Astrophysics Science Archive Research Center. HEASARC is an archive for collecting data of high energy electromagnetic radiation from different sources. HEASOFT contains many software packages, like FTOOLS, XANADU, etc. In this thesis, XANADU software has been mainly used. XANADU contains three different programmes for three different purposes:

1) XRONOS - for timing analysis

2) XSPEC - for spectral analysis

3) XIMAGE - for imaging

   For more information, (*XANADU Software Home Page* 2003)

3.2 XRONOS

XRONOS is an X-Ray timing analysis package available in the HEASOFT software. It is detector and wavelength independent.

   lcurve comes under the package of XRONOS. It is used to plot lightcurves. It reads the .lc file and plots it using the plotting software QDP Plot. Lightcurves are brightness vs time diagrams. It allows us to study the change in the brightness of different sources in due course of time. For example, take the case of an eclipsing binary star system, that

is a system where the orbital plane lies nearly along the line of sight, such that one star eclipses the other. In such a system, its period can be found out using lightcurves. 'lcurve' is also used to make hardness ratio diagrams between two energy bands, that is ratio of flux of two energy bands versus time.
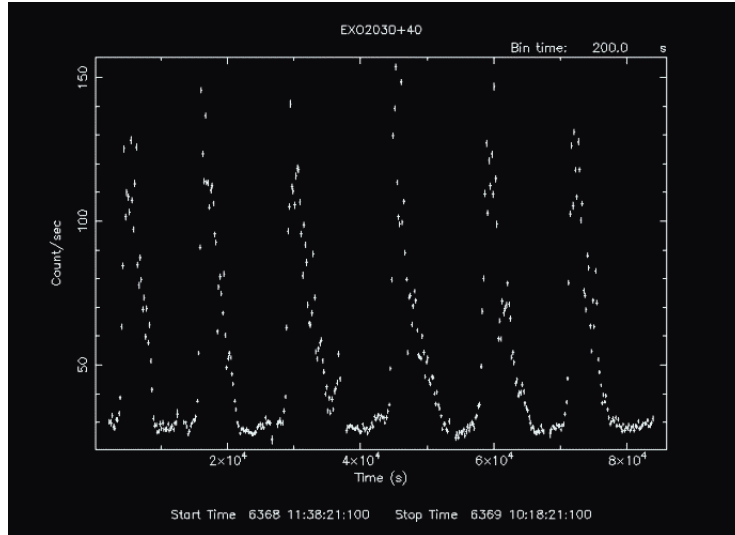
Figure 3.1: A sample light curve using lcurve. Image from (*NASA's HEASARC Software 2004*)

3.3 XSPEC

3.3.1 Working of XSPEC

In spectral analysis we fit data using different models that comes with the XSPEC package. We can decide on the goodness of fit using a character called fit statistic. Chi-square analysis is an example of a fit statistic. It is given by (Bevington et al., 1993):

$$\chi^2 = \frac{\sum (counts_{observed} - counts_{calculated})^2}{\sigma^2} \tag{3.1}$$

Once we get the χ^2 value or rather the reduced χ^2 value, which is χ^2 divided by degrees of freedom(number of channels - number of model parameters). Generally a χ^2 value close to 1 is considered a good fit. After getting the fit statistic, we find the best fit parameters by trial and error of changing a particular model parameter after freezing the rest.

For a single spectrum analysis we may require four files : a source file, a background file, a response file and an arf (auxiliary response file). The source file contains the information on the photon counts detected by the specific instrument in a given channel and the background file is used to subtract from it to get the final spectra. The response file has the instrument/detector response and the arf file is related to it.

The three files - background, response and arf file can be added to the data file using the tool GRPPHA.

From the XPSEC manual, we get the formula for background subtracted spectra :

$$C(I) = \frac{D(I)}{a_{D(I)} * t_D} - \frac{b_{D(I)}}{b_{B(I)}} * \frac{B(I)}{a_{B(I)} * t_B} \tag{3.2}$$

where $D(I)$ is counts in data file, $B(I)$ is counts in background file, t_D, t_B are exposure time and $b_{D(I)}, b_{B(I)}, a_{B(I)}, a_{D(I)}$ are background and area scaling values respectively

The instrumental response, $R(I, E)$ is related to the probability that a photon of particular energy will be detected in a particular channel. This response is discretised into a response matrix. In order to take care of the efficiency of the detector, an array of values called auxiliary response file is multiplied into what we call the rmf or redistribution matrix function. This is the reason, we have two separate files for response - .rmf and .arf

The models used in spectral analysis are :

3.3.2 Models Used

'tbabs' model

There has been an update to the photo-ionisation cross section and abundances of the Interstellar Medium. Many papers have been cited on computing σ_{ISM} (photo-ionisation cross section) by allowing to adjust the abundances of the ISM and using polynomial fits

to the cross sections. See (Wilms, Allen, and McCray, 2000)

The photo-ionisation cross section, σ_{ISM} is given by :

$$\sigma_{ISM} = \sigma_{gas} + \sigma_{mol} + \sigma_{grain}$$

σ_{ISM} is normalised to the total hydrogen number density N_H, thus giving the X-Ray spectra as :

$$I_{obs}(E) = e^{-\sigma_{ISM}(E)N_H} I_{source}(E) \tag{3.3}$$

1) Gaseous contribution to the ISM :

It is obtained by adding the photo-ionisation cross sections of individual atoms and ions in these phases and weighing the contributions by the abundances. So :

$$\sigma_{gas} = \sum A_Z a_{Z,i}(1 - \beta_{Z,i})\sigma_{bf}(Z,i) \tag{3.4}$$

where A_Z is the abundance in the number of element Z with respect to hydrogen and is given by :

$$A_Z = \frac{N(Z)}{N(H)} \tag{3.5}$$

and $a_{Z,i}$ being the fraction of ions of element Z in stage i and $\sigma_{bf}(Z,i)$ is total photoionisation cross section of element Z in ionisation stage i and $(1 - \beta_{Z,i})$ being the depletion of the elements to grains

2) Molecular Contribution :

Since molecular hydrogen H_2 has large abundance, only that is considered. So:

$$\sigma_{mol} = A_{H_2}\sigma_{bf}(H_2) \tag{3.6}$$

3) Grain contribution :

Since the X-Ray optical depth of a large grain can be much greater than 1, X-Ray absorption mainly happens at its surface and thus the contribution of material within the grain to σ_{ISM} is small.

Updates in abundances :

The elemental abundances are important for getting the value of σ_{ISM}. The abundance for gas and dust model for ISM is difficult. Thus solar abundances were used as a reference abundance for ISM. Solar abundance is determined from analysis of solar photosphere or meteorites.

'tbabs' is the Tuebingen-Boulder ISM absorption model. As described above, tbabs calculates the total X-Ray absorption cross-section by ISM by including the contributions from gas, grains and molecules in the interstellar medium. For tbabs, there is only one parameter and that is, the n_H or the hydrogen column density. Since absorption occurs anywhere near the line of sight, the column density is used. The parameter is given by :

par1 = n_H (in terms of 10^{22} atoms/cm^2)

'edge' model

This is used for modelling an absorption edge. It is given by :

$$M(E) = 1, \quad E \leq E_c \tag{3.7}$$

$$M(E) = exp[-D(\frac{E}{E_c})^{-3}], \quad E \geq E_c \tag{3.8}$$

'powerlaw' model

It is of the form,

$$A(E) = KE^{-\alpha} \tag{3.9}$$

where α is the photon index and K is the norm which has the units of photons/keV/cm^2/s

3.4   NuSTARDAS

NuSTARDAS(NuSTAR Data Analysis Software) processes data in three steps :

1) Data Calibration

2) Data Screening

3) Product Extraction

Data is calibrated using CALDB files. The first stage in data extraction is done in the nupipeline tool with the following command :

nupipeline indir=/disk/nustar/archive/10012001002/

outdir=./out

steminputs=nu10012001002

After completing stage 1 and 2, we perform stage 3, that is, the extraction. Two event files are obtained, that is for FPMA and FPMB(Focal Point Module A and B). The image of the X-Ray events, generated from the two stages allow us to observe the X-Ray photons from the celestial source, provided the exposure time is sufficient. The software, DS9 is used to view the image of the event. A source extraction region file is made, using DS9 by selecting a circular region centered on the source and saving it. Similarly a background region file is also created by selecting the region just outside the source photons. Then stage 3, that is extracting light curves and spectrum is performed by using the 'nuproducts' command. Its done for both FPMA and FPMB instruments.

3.5 Timing Analysis

3.5.1 Swift Data

The lightcurve data from the Swift Observatory has been obtained from the SWIFT BAT(Burst Alert Telescope) Hard X-Ray Transient Monitor. The data is starting from MJD 57101 (March 2015) to MJD 58485 (February 2018). The source of the X-Ray light curve is (*Swift/BAT Hard X-ray Transient Monitor* 2019) and (Krimm et al., 2013)

3.5.2 MAXI Data

The data for the MAXI Light Curves were obtained from their official site. The data is in the 2-20 keV band. Also, data was available in three different bands : 2-4 keV, 4-10 keV and 10-20 keV. For the source of the lightcurves, see (Matsuoka et al., 2009) and (RIKEN, JAXA, and team, 2019)

The Swift and MAXI light curves are plotted here along with the optical light curves for comparison.

The light curves of Cyg X-3 are in the order :

1) Swift light curves

2) Maxi light curves in the energy range(2-20 keV)

3) 2-4keV MAXI light curves

4) 4-10keV MAXI light curves

5) 10-20keV MAXI light curves

The light curves start from MJD 57101 to 58485. The four vertical dashed lines have divided the plots to different intervals. This division is for the better viewing of the peaks and dips in the lightcurve. For data analysis in case of Swift, count rates with error < 0.0031 were filtered and for MAXI, only those data points were selected whose signal to noise ratio was greater than 5

Comparing the full Swift and MAXI light curves, we can see that for a peak in the SWIFT light curve, correspondingly there is a dip in the MAXI light curve and vice versa
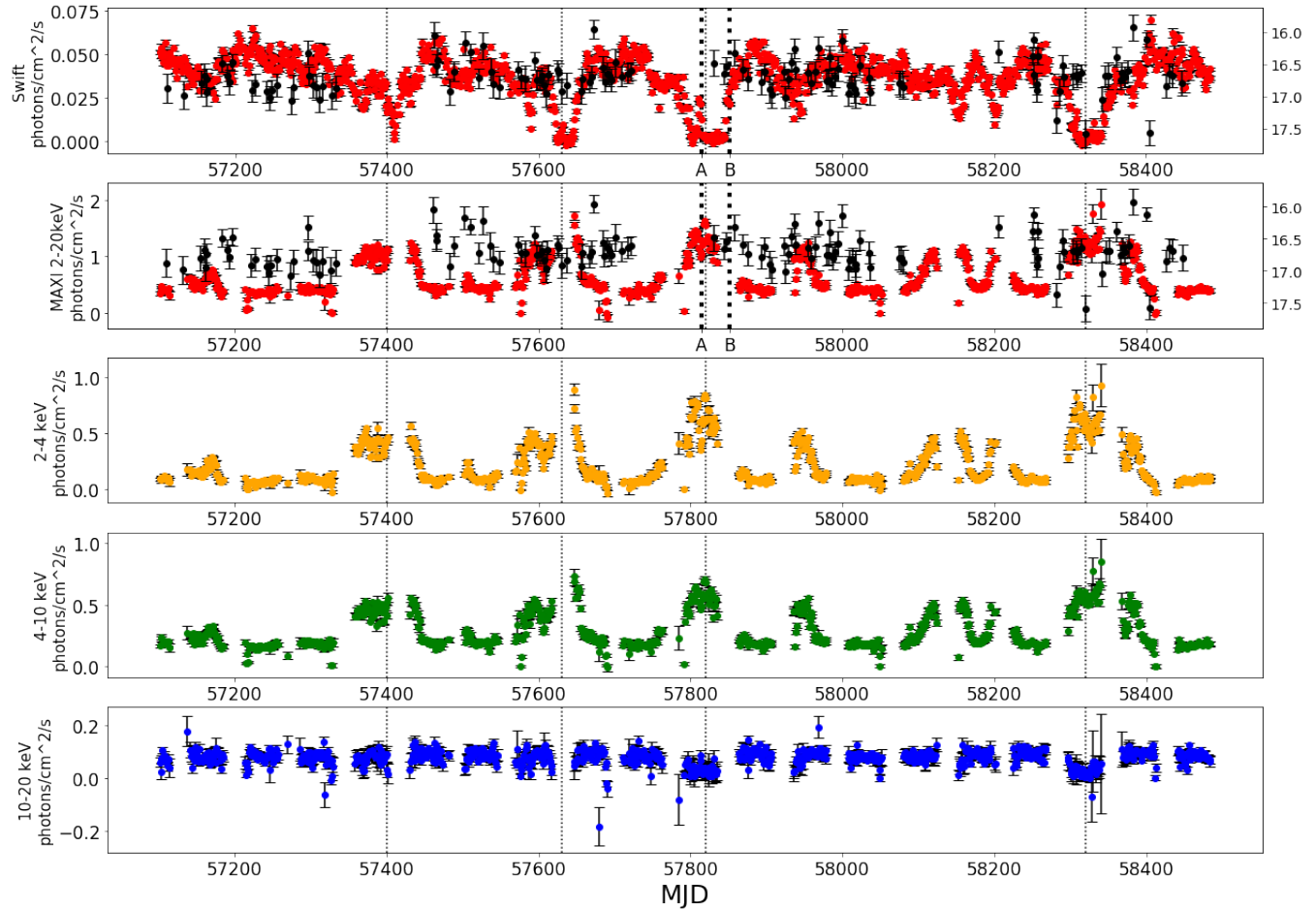
Figure 3.2: Swift and MAXI Light curves. The black labels mark the optical lightcurves in the first and second plots and the right y-axis is of optical magnitude. 'A' and 'B' refers to the NuSTAR pointed observations on MJD 57814 and MJD 57851

In the first phase, we see an almost steady count rate which dips down to almost zero at MJD 57400. From MJD 57400, we see a peak at approx. 57450 and it dips down at nearly MJD 57620. From MJD 57620, again we see a peak at nearly 57700. In the next phase we see high count rates which again is almost steady until MJD 58300 where it dips to nearly 0

For hardness ratio, only MAXI data were used, that of three bands :
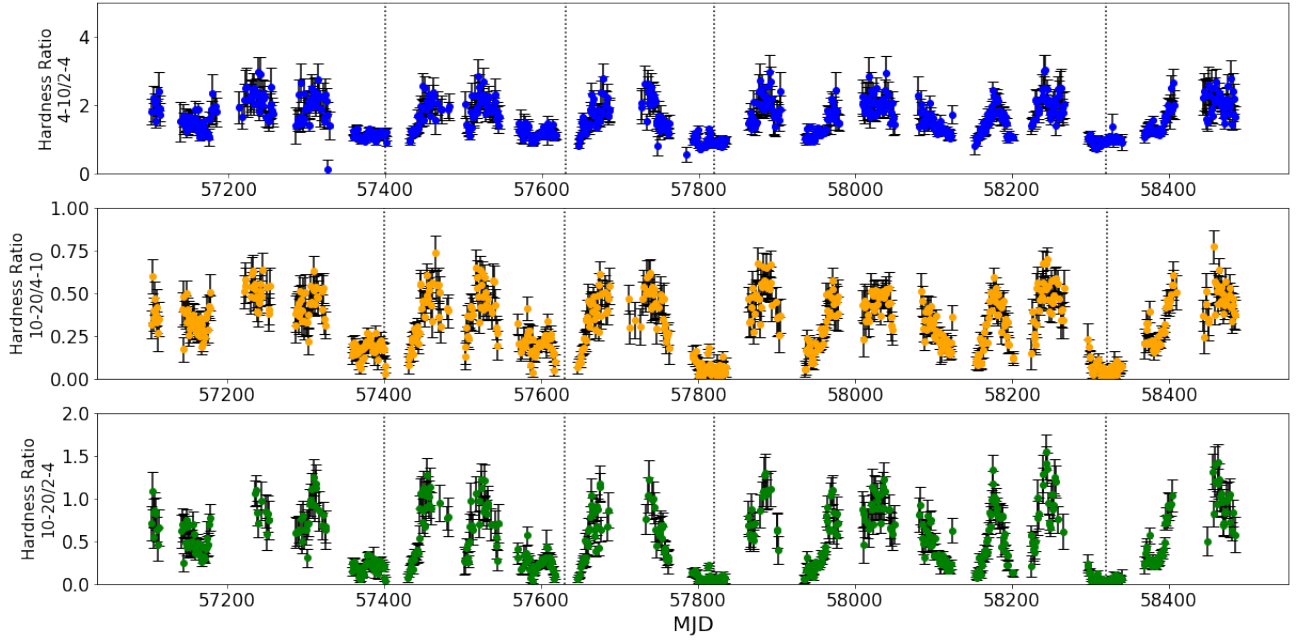
1) 2 - 4 keV

2) 4 - 10 keV

Figure 3.3: MAXI Hardness Ratio

3) 10 - 20 keV

For 4-10/2-4 HR, we see HR > 1 for most of the time, even more than 5 times the average value of HR(1.77) in this case. For 10-20/4-10 HR, HR only shoots up to greater than 1 very rarely, at MJD 57200 and MJD 57240 and also at nearly MJD 57700. The motivation of this project is to study the spectral evolution for a time period of three years and to see any correspondence between the possible origin of soft and hard X-Ray components.

From the optical lightcurves, we see that irrespective of the spectral evolution, we see no variability on the optical magnitudes. The source was found to be optically bright throughout during the period of three years from 2015. From the hardness ratio plots we observe that the soft X-Ray flux has large count rates and hard X-Ray flux has low count rates. This state is described by a hypersoft state in (Koljonen et al., 2018)

3.6   Spectral Analysis

NuSTAR Data was obtained for pointed observations on MJD 57814 (2 March 2017) and on MJD 57851 (8 April 2017). The data was downloaded from NuSTAR Archive available online (See Myers, 2019). This data was extracted using the NuSTARDAS(NuSTAR Data

Analysis Software) tool - nupipeline. For extracting lightcurves and spectra, the 'nuproducts' command was used. Using DS9, a circular region of 60 arcseconds was selected as source and for background, a circular region of 90 arcseconds just outside the source was selected.

NuSTAR Observation ID	Start Date	Exposure Time[s]
90202051002	2017-03-02 05:26:09	14538
90202051004	2017-04-08 22:51:09	14538

Table 3.1: Table of NuSTAR Observations

Since, the X-ray light curves obtained with NuSTAR showed a large variability, for obtaining the spectra, Good Time Intervals (GTIs) of the light curve on MJD 57814 were selected with an interval of 1000 seconds, starting from 0 to 38000s. Therefore, spectra were extracted for these GTIs, i.e. a total of 23 spectra(both background and source file). Using the GRPPHA tool, available in HEASOFT, these spectra were grouped for a minimum count rate of 25 counts/s. Then spectral fitting was done for each of the spectra.
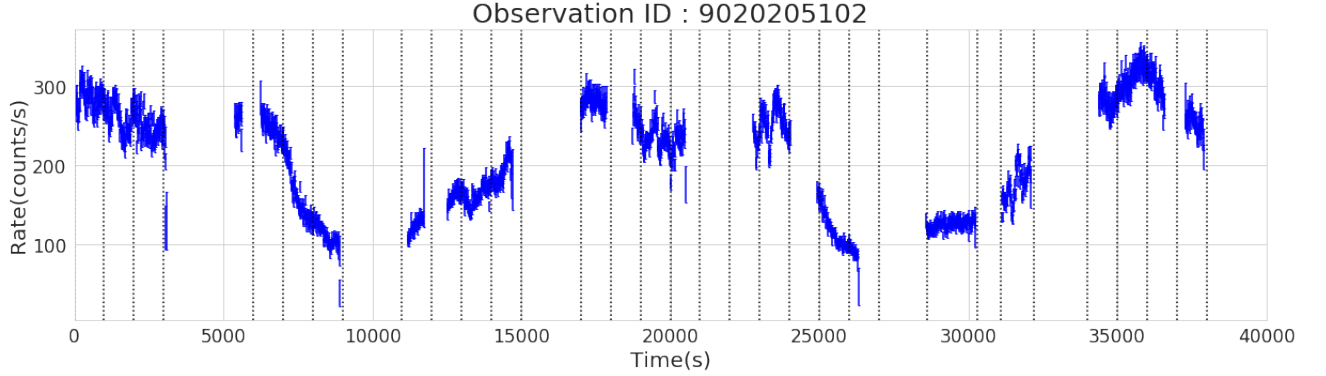

Figure 3.4: NuSTAR Pointed Observation on MJD 57814
Observation ID : 90202051002

The XSPEC tool of HEASOFT was used for the spectral fitting of the spectra obtained from the NuSTAR pointed observation mentioned before. The model used for spectral fitting was :

TBabs(edge*edge(gaussian + bbodyrad)+ powerlaw)

For the description of the individual components of the model, see Section 3.3.2. One
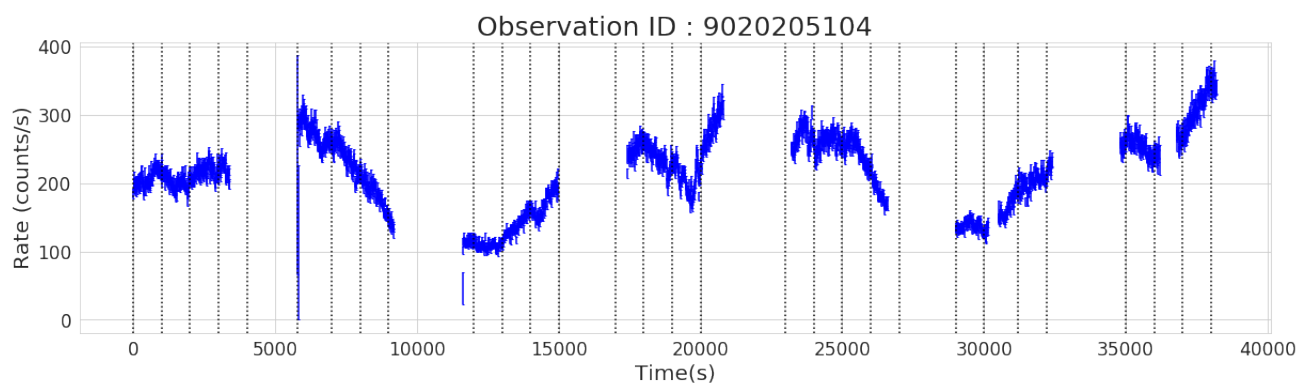
Figure 3.5: NuSTAR Pointed Observation on MJD 57851

Observation ID : 90202051004

of the sample spectrum is shown here :
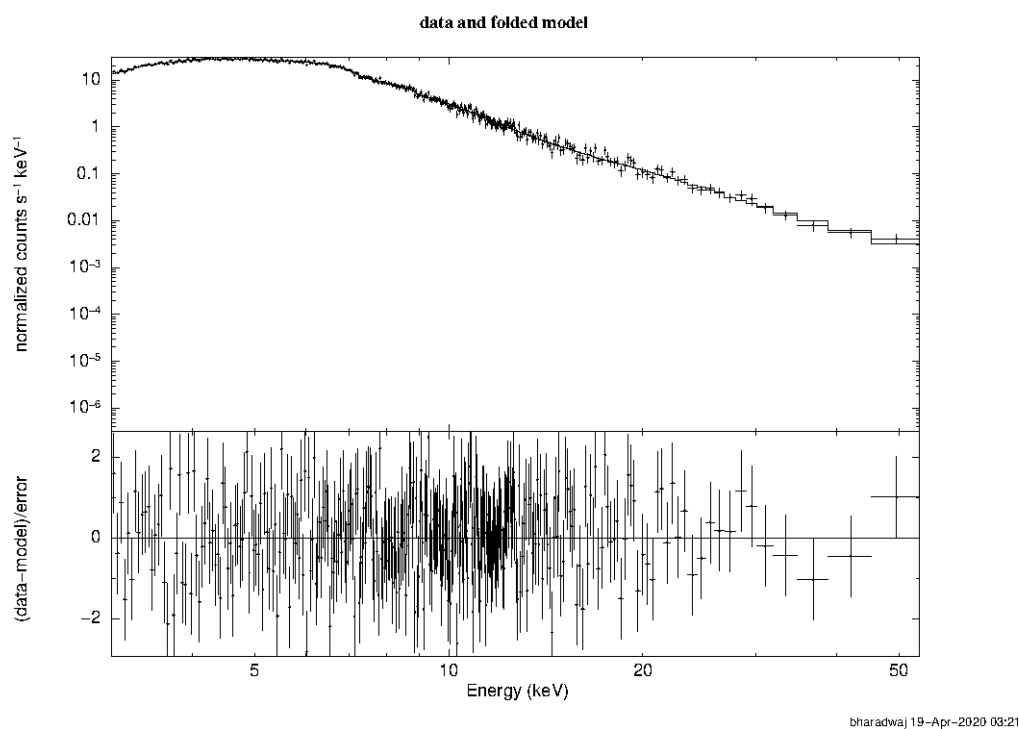

Figure 3.6: Extracted spectrum from the interval 2000 to 3000 seconds along with the residual plot.

Observation ID : 90202051002

Using the long term Swift and MAXI light curves, we can say that this pointed observation was performed during its hypersoft spectral state (Koljonen et al., 2018). When the source, is in the hypersoft state, obviously, the spectrum is soft. The X-Ray spectra
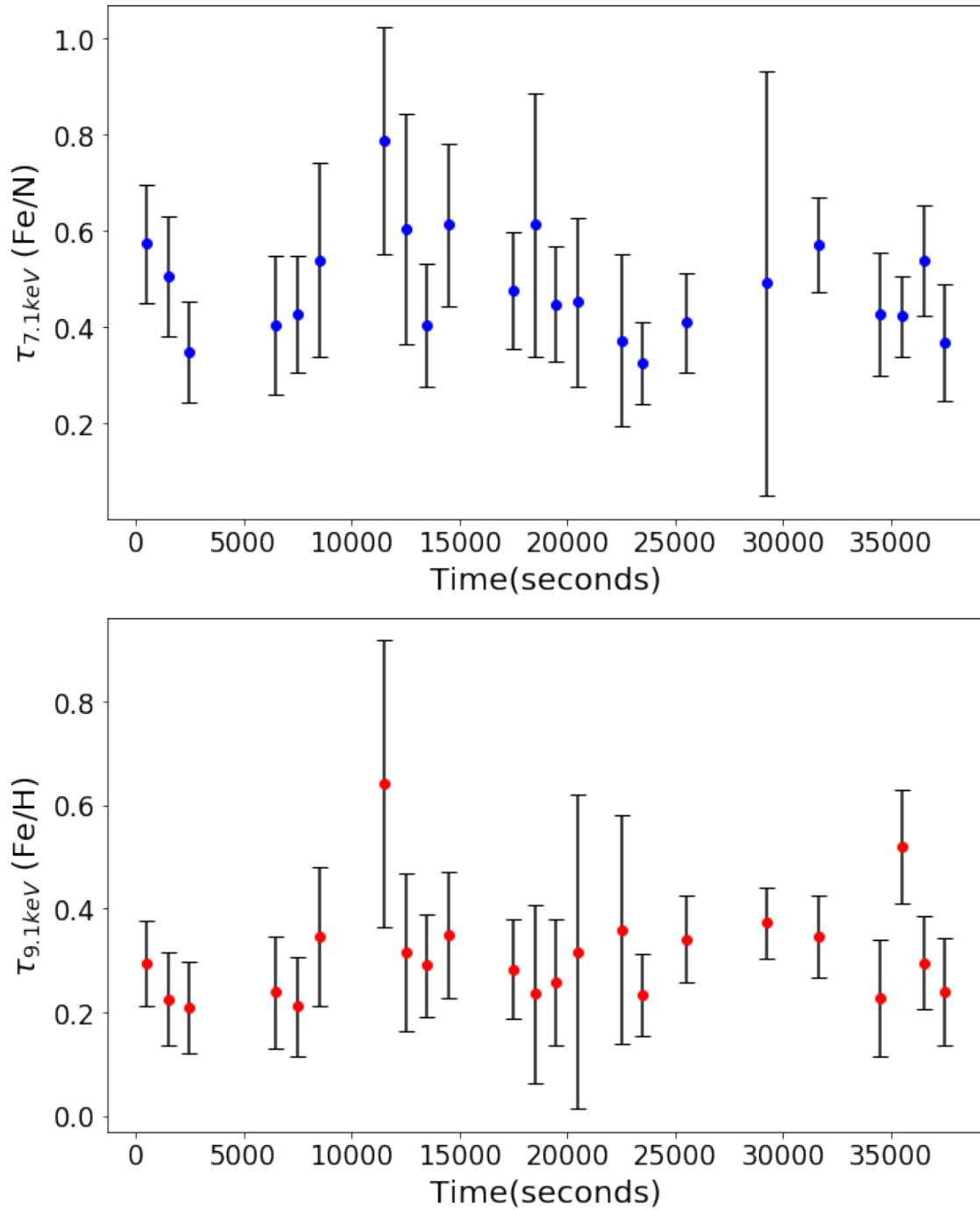
Figure 3.7: Parameter evolution over time. Top : Optical Depth of Neutral Iron. Bottom : Optical Depth of H-like Iron.

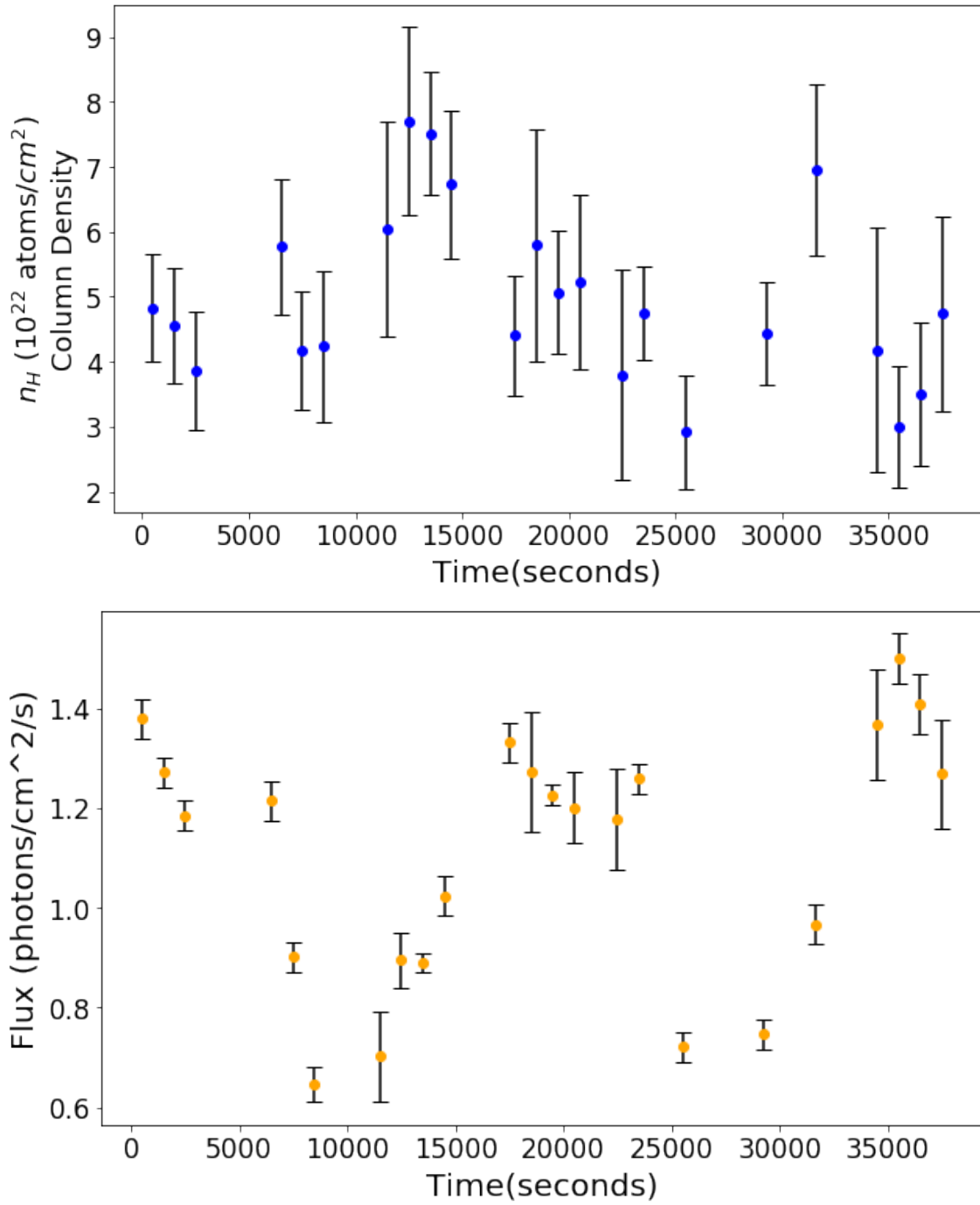NuSTAR Observation ID : 90202051002

Figure 3.8: Parameter evolution over time. Top : The hydrogen column density. Bottom : Total flux in the 3-79 keV band
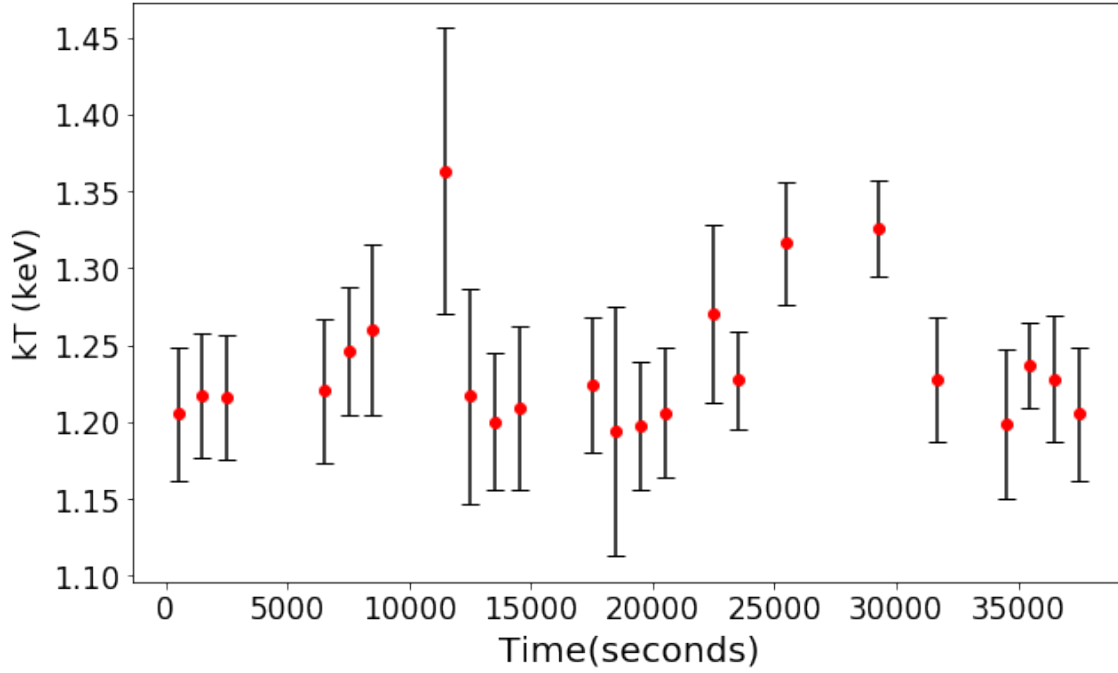
NuSTAR Observation ID : 90202051002

Figure 3.9: Evolution of the parameter - kT (blackbody temperature)
NuSTAR Observation ID : 90202051002

after splitting into time intervals of 1ksec were modelled using a single temperature radiating blackbody and a powerlaw component, attenuated by interstellar absorption(TBabs model). The reason for including the 'powerlaw' comes from the Compton upscattering of photons radiating from the blackbody due to high energy electrons or it may come from the Compton upscattering of infrared photons present in the jet of the microquasar. Also, we added an iron line complex('gaussian') and absorption edges of neutral and highly ionised iron. The two absorption edges that were added are of neutral iron (Fe/N) at energy around 7.1 keV and the hydrogen-like iron (Fe/H) at energy around 9.1 keV. The evolution of parameters over time is depicted in the figures, Fig 3.8, 3.6 and 3.9

We got acceptable fits using this model. Error was calculated in the 90% range. The blackbody temperature fluctuated around 1.1 - 1.4 keV. The neutral iron absorption edge was in the range 6.8 - 7.4 keV and the hydrogen-like edge was in the range 8.7 - 9.3 keV and its optical depth remained mainly between 0.05 to 0.2 regime. The photon index stayed in the 2 - 3 range.

Parameter	Component	Parameter Name	Value	Error
1	TBabs	nH	3.86	+0.96, -0.87
2	edge	edgeE	8.88	+0.11, -0.10
3	edge	τ_{max}	0.35	+0.11, -0.10
4	edge	edgeE	7.14	+0.10.17, -0.13
5	edge	τ_{max}	0.21	+0.08, -0.09
6	gaussian	LineE	6.44	+0.13, -0.13
7	gaussian	Sigma	0.4	-
8	gaussian	norm	1.96	+0.00, -0.00
9	bbodyrad	kT	1.22	+0.04, -0.04
10	bbodyrad	norm	548.97	+87.76, -71.01
11	powerlaw	Photon Index	2.48	+0.20, -0.19
12	powerlaw	norm	2.38	+1.97, -1.08

Table 3.2: A sample set of parameters for the spectrum of the time interval 2000 to 3000 seconds where reduced $\chi^2 = 1.0259$ for 303 d.o.f.
NuSTAR Observation ID : 90202051002

3.7 Summary of Results

- For the source, Cygnus X-3 long term optical lightcurve has been obtained from All Sky Automated Survey for SuperNovae(ASAS-SN) and X-Ray lightcurves from Swift Burst Alert Telescope and Monitor of All-Sky X-Ray Image(MAXI) to understand the long term spectral evolution of Cyg X-3. The lightcurves were from MJD 57101 (March 2015) to MJD 58485 (February 2019).

- A model-independent way using hardness ratio plots was used for this purpose.

- An anti-correlation was established between the soft (0.1 - 10 keV) X-Rays and hard (10 - 100keV) X-Rays.

- The optical emission was independent of the above correlation. The source remained optically bright throughout the three years of observation from 2015 (between the magnitude of 16 - 17)

- From the archive of the Nuclear Spectroscopic Telescope Array (NuSTAR), pointed observations on MJD 57814 (2 March 2017) and MJD 57851 (8 April 2017) were extracted. Due to large variability in X-Rays lightcurves, time resolved spectroscopy was performed for the pointed observation on MJD 57814.

- From the long-term lightcurves, we know that the source is in the hypersoft spectral state.

- For spectral analysis a model consisting of a single temperature radiating blackbody has been used along with a powerlaw component which is attenuated by interstellar absorption. It was fitted for 18 different spectra of 1 ksec each

- Iron emission lines and absorption edges of neutral and ionised iron were also observed in the spectra.

- There was no significant variation in the neutral hydrogen column density, optical depths of absorption edges found in these X-ray spectra, however, X-ray flux showed a large variation across different spectra extracted during different times. There was some variation observed in the blackbody temperature as well.

3.8   Future Plans

Our spectral results showed the presence of a large variability in the X-ray flux, indicating the evolution of the accretion geometry. In order to obtain physical insights into the geometry of this source, we aim to perform more careful and comprehensive spectral study of this source using all available NuSTAR observations.

Bibliography

Bevington, Philip R et al. (1993). "Data reduction and error analysis for the physical sciences". In: *Computers in Physics* 7.4, pp. 415–416.

Blondin, John M et al. (1990). "Hydrodynamic simulations of stellar wind disruption by a compact X-ray source". In: *The Astrophysical Journal* 356, pp. 591–608.

Brandt, Niel (2019). *X-Ray spectrum*. URL: `https://personal.psu.edu/wnb3/astro485/lectures/lecture07-overhead01.jpg`.

Carroll, Bradley W and Dale A Ostlie (2017). *An introduction to modern astrophysics*. Cambridge University Press.

Dickey, John M (1983). "A new distance to Cygnus X-3". In: *The Astrophysical Journal* 273, pp. L71–L73.

Electromagnetic Spectrum - Introduction (2013). URL: `https://imagine.gsfc.nasa.gov/science/toolbox/emspectrum1.html`.

Fender, Robert P, MM Hanson, and Guy G Pooley (1999). "Infrared spectroscopic variability of Cygnus X-3 in outburst and quiescence". In: *Monthly Notices of the Royal Astronomical Society* 308.2, pp. 473–484.

Frank, Juhan, Andrew King, Derek Raine, et al. (2002). *Accretion power in astrophysics*. Cambridge university press.

Hjalmarsdotter, Linnea et al. (2009). "Spectral variability in Cygnus X-3". In: *Monthly Notices of the Royal Astronomical Society* 392.1, pp. 251–263.

Kochanek, CS et al. (2017). "The all-sky automated survey for supernovae (ASAS-SN) light curve server v1. 0". In: *Publications of the Astronomical Society of the Pacific* 129.980, p. 104502.

Koljonen, KII et al. (2018). "The hypersoft state of Cygnus X–3-A key to jet quenching in X-ray binaries?" In: *Astronomy & Astrophysics* 612, A27.

Krimm, Hans A et al. (2013). "The Swift/BAT hard X-ray transient monitor". In: *The Astrophysical Journal Supplement Series* 209.1, p. 14.

Ling, Samuel J., Jeff Sanny, and William Moebs (2016). *Blackbody Radiation - University Physics Volume 3*. URL: `https://openstax.org/books/university-physics-volume-3/pages/6-1-blackbody-radiation`.

Longair, Malcolm S (2011). *High energy astrophysics*. Cambridge university press.

Matsuoka, Masaru et al. (2009). "The MAXI mission on the ISS: science and instruments for monitoring all-sky X-ray images". In: *Publications of the Astronomical Society of Japan* 61.5, pp. 999–1010.

McClintock, Jeffrey E and Ronald A Remillard (2003). "Black hole binaries". In: *arXiv preprint astro-ph/0306213*.

Myers, J D (2019). *HEASARC NuSTAR Archive*. URL: `https://heasarc.gsfc.nasa.gov/docs/nustar/`.

NASA's HEASARC Software (2004). URL: `https://heasarc.gsfc.nasa.gov/docs/xanadu/xronos/examples/lcurve.html`.

Optics (2019). URL: `https://www.nustar.caltech.edu/page/optics`.

Optics (2019). URL: `https://www.nustar.caltech.edu/page/optics`.

Parsignault, DR et al. (1972). "Observations of Cygnus X-3 by Uhuru". In: *Nature Physical Science* 239.95, pp. 123–125.

Rajeev, M. R. et al. (Mar. 1994). "Generalized Spectral Model for 1–100 keV X-Ray Emission from Cygnus X-3 Based on EXOSAT Data". In: 424, p. 376. DOI: `10.1086/173896`.

Remillard, Ronald A and Jeffrey E McClintock (2006). "X-ray properties of black-hole binaries". In: *Annu. Rev. Astron. Astrophys.* 44, pp. 49–92.

RIKEN, JAXA, and MAXI team (2019). URL: `http://maxi.riken.jp/top/index.html`.

Schmutz, W., T. R. Geballe, and H. Schild (Jan. 1996). "Cyg X-3: evidence for a black hole." In: 311, pp. L25–L28.

Seward, Frederick D and Philip A Charles (2010). *Exploring the X-ray Universe*. Cambridge University Press.

Shappee, Benjamin J et al. (2014). "The man behind the curtain: X-rays drive the UV through NIR variability in the 2013 active galactic nucleus outburst in NGC 2617". In: *The Astrophysical Journal* 788.1, p. 48.

Swift: About Swift - BAT Instrument Description (2014). URL: `https://swift.gsfc.nasa.gov/about_swift/bat_desc.html`.

Swift: About Swift - UVOT Instrument Description (2014). URL: `https://swift.gsfc.nasa.gov/about_swift/uvot_desc.html`.

Swift: About Swift - XRT Instrument Description (2016). URL: `https://swift.gsfc.nasa.gov/about_swift/xrt_desc.html`.

Swift/BAT Hard X-ray Transient Monitor (2019). URL: `https://swift.gsfc.nasa.gov/results/transients/`.

Szostek, Anna and AA Zdziarski (2005). "A study of spectra of Cyg X-3 observed by BeppoSAX". In: *AIP Conference Proceedings*. Vol. 774. 1. American Institute of Physics, pp. 341–343.

Wilms, J, A Allen, and R McCray (2000). "On the absorption of X-rays in the interstellar medium". In: *The Astrophysical Journal* 542.2, p. 914.

XANADU Software Home Page (2003). URL: `https://heasarc.gsfc.nasa.gov/docs/xanadu/xanadu.html`.